Nanoimprinting-Induced Nanomorphological Transition in Polymer Solar Cells: Enhanced Electrical and Optical Performance

Seonju Jeong,[†,‡] Changsoon Cho,[†,‡] Hyunbum Kang,[§] Ki-Hyun Kim,[§] Youngji Yuk,[†] Jeong Young Park,[†,∥] Bumjoon J. Kim,[*,§] and Jung-Yong Lee[*,†,‡]

[†]Graduate School of Energy, Environment, Water, and Sustainability (EEWS), [‡]Graphene Research Center, [§]Department of Chemical and Biomolecular Engineering, and [∥]Center for Nanomaterials and Chemical Reactions, Institute for Basic Science (IBS), Korea Advanced Institute Science and Technology (KAIST), Daejeon 305-701, Republic of Korea

ABSTRACT We have investigated the effects of a directly nanopatterned active layer on the electrical and optical properties of inverted polymer solar cells (i-PSCs). The capillary force in confined molds plays a critical role in polymer crystallization and phase separation of the film. The nanoimprinting process induced improved crystallization and multidimensional chain alignment of polymers for more effective charge transfer and a fine phase-separation between polymers and [6,6]-phenyl-C_{71}-butyric acid methyl ester ($PC_{71}BM$) to favor exciton dissociation and increase the generation rate of charge transfer excitons. Consequently, the power conversion efficiency with a periodic nanostructure was enhanced from 7.40% to 8.50% and 7.17% to 9.15% in PTB7 and PTB7-Th based i-PSCs, respectively.

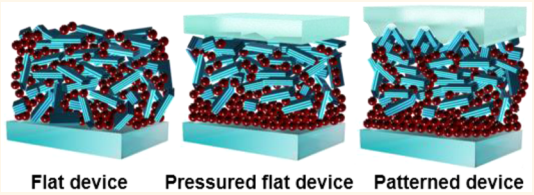

KEYWORDS: inverted polymer solar cell · phase segregation · periodic nanostructure · nanoimprinting · nanomorphology

Polymer solar cells (PSCs) have received considerable attention as next-generation solar cells that can be applied to portable electronic devices such as tablets, laptops, and cellular phones due to their advantages of transparency, lightweightiness, and flexibility. Although the power conversion efficiency (PCE) of PSCs has seen a dramatic increase in the past few years and has reached nearly 10%,[1] there is still need for enhancing their PCE further to be commercially viable. Previous studies have mostly focused on developing new active materials to improve the efficiency of PSCs.[2,3] However, in order to extract the full potential from given active materials, device structure needs to be optimized to enhance the optical performance as well as electrical properties.

Better crystalline nature of the donor polymer, smaller and better dispersed domains of the acceptor fullerene derivative, and favorable phase separation between the donor and acceptor with continuous pathways facilitate enhanced charge transport properties of blend films.[4,5] Furthermore, proper vertical phase segregation for electrode selectivity, in which donor and acceptor materials are preferred toward the anode and cathode, respectively, can improve charge transport and collection.[6,7] Electrical properties in PSCs are reportedly related with the process of exciton dissociation at the interfaces between donors and acceptors,[4,8] diffusion of charge carriers,[5,9] and charge collection at each electrode.[10,11] Controlling the nanomorphology in the blend film is thus very important to promote the electrical properties in the PSCs.[12,13]

Nanomorphology within a blend film can be controlled by various approaches, including thermal and solvent annealing,[6,14] control of the solvent evaporation rate,[15] and the use of processing additives such as 1,8-diiodooctane (DIO) and 1,8-octanedithiol (ODT) for selective solubility.[16,17] It is well-known that the nanomorphology of polymer blend films can be controlled by adjusting the crystallization of the polymer.[18−20] For example, when a solvent is

* Address correspondence to jungyong.lee@kaist.ac.kr, bumjoonkim@kaist.ac.kr.

Received for review November 23, 2014 and accepted February 17, 2015.

Published online February 17, 2015
10.1021/nn506678a

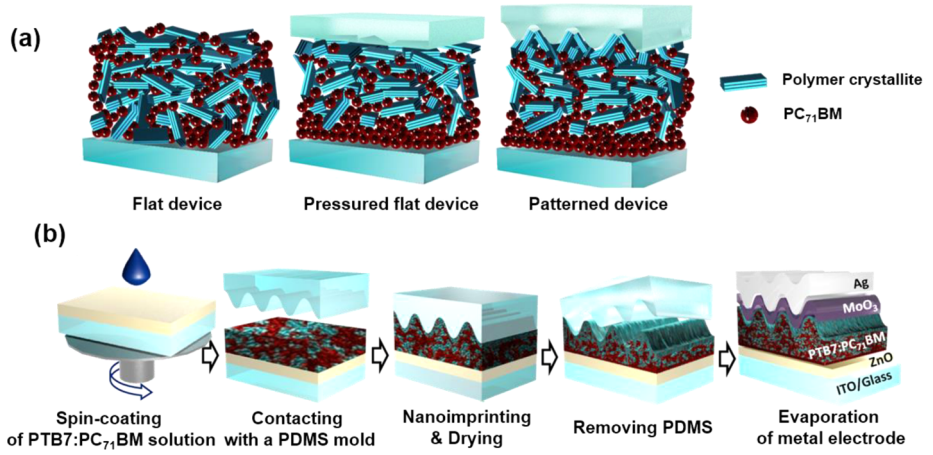

Figure 1. Effect of nanoimprinting and fabrication process: (a) the proposed mechanism of vertical phase separation induced by the nanoimprinting process and (b) the nanoimprinting process to induce nanomorphological change and the device structure of i-PSCs with a periodic nanostructure.

more slowly evaporated, the polymer crystal is more uniform and phase separation between polymer crystallite structures and acceptor domains is effectively formed, which is favorable for exciton dissociation.[19,21]

The use of periodic metallic nanostructures has recently become one of the favored schemes to improve the performance of PSCs. Introduction of periodic metallic nanostructures into PSCs has often targeted optical absorption enhancement via surface plasmon resonance (SPR) effects near specific resonant wavelengths.[22,23] Moreover, it has been recently reported that random wrinkles in PSCs can significantly enhance the photoresponse in the NIR region due to effective direct formation of hot charge transfer excitons (CTXs) and additional wave guiding effects into the active layer to increase the path length of the NIR photons.[24] These results imply that the appropriate introduction of nanostructures in PSCs can efficiently boost the absorption of NIR photons due to increased generation of CTXs despite intrinsic low absorption in this range.[25,26]

Meanwhile, there have been few studies on the effects on electrical properties of the incorporation of periodic metallic nanostructures into PSCs. In the present study, we demonstrate a nanoimprinting process can induce a dramatic nanomorphological change of the bulk active layer of the PSCs, effectively improving electrical properties as well as optical performance in inverted polymer solar cells (i-PSCs). In the nanoimprinting process, a concentrated solution containing organic materials filled the periodic nanomold by capillary pressure and the solvent was evaporated slowly; the materials were solidified or crystallized while confined in the molds.[27,28] The capillary force in the nanoimprinting process plays roles in polymer crystallization and phase separation of the film. After the solvent reaches a critical volume, crystallites of the polymer grow and pack orderly by the upward driving force of the capillary force.[29,30] Figure 1a schematically illustrates the morphological transition induced by the proposed nanoimprinting process. In our experiments, the incorporation of periodic nanostructures on poly[[4,8-bis[(2-ethylhexyl)oxy]benzo[1,2-b:4,5-b']-dithiophene-2,6-diyl][3-fluoro-2-[(2-ethylhexyl)carbonyl]-thieno[3,4-b]thiophenediyl]] (PTB7):(6,6)-phenyl C71-butyric acid methyl ester ($PC_{71}BM$) and poly[4,8-bis(5-(2-ethylhexyl)thiophen-2-yl)benzo[1,2-b;4,5-b']dithiophene-2,6-diyl-alt-(4-(2-ethylhexyl)-3-fluorothieno[3,4-b]-thiophene-)-2-carboxylate-2-6-diyl)] (PTB7-Th):$PC_{71}BM$ increases the power conversion efficiency (PCE) by approximately 15% and 28%, respectively. We discuss the origin of the enhanced electrical properties, such as internal quantum efficiency (IQE) and fill factor (FF), upon the introduction of periodic nanostructures.

RESULTS AND DISCUSSION

A simple nanoimprinting method using a polydimethylsiloxane (PDMS) mold was applied to induce a nanostructured pattern onto the surface of an active layer consisting of PTB7 and $PC_{71}BM$. Figure 1b schematically illustrates the fabrication process of the periodically nanostructured i-PSC devices. The as-spun PTB7:$PC_{71}BM$ layer was immediately contacted with a patterned PDMS mold (period, 556 nm) and then dried on a hot plate under the pressure of 52.95 Pa. Fabrication details for the PDMS mold and devices are presented in the Methods. A mold with a depth of 40 nm and period of 556 nm was prepared and applied to fabricate nanopatterned i-PSC devices. Figure 2a provides a cross-sectional scanning electron microscopy (SEM) image of the device with the patterned active layer comprising PTB7 and $PC_{71}BM$, exhibiting a periodically structured surface. It confirms that periodic patterns have been successfully formed on the surface of the active layer by the nanoimprinting process.

The photovoltaic performance of i-PSCs with periodic nanostructures was investigated to assess the effect of the periodic nanostructures, as summarized

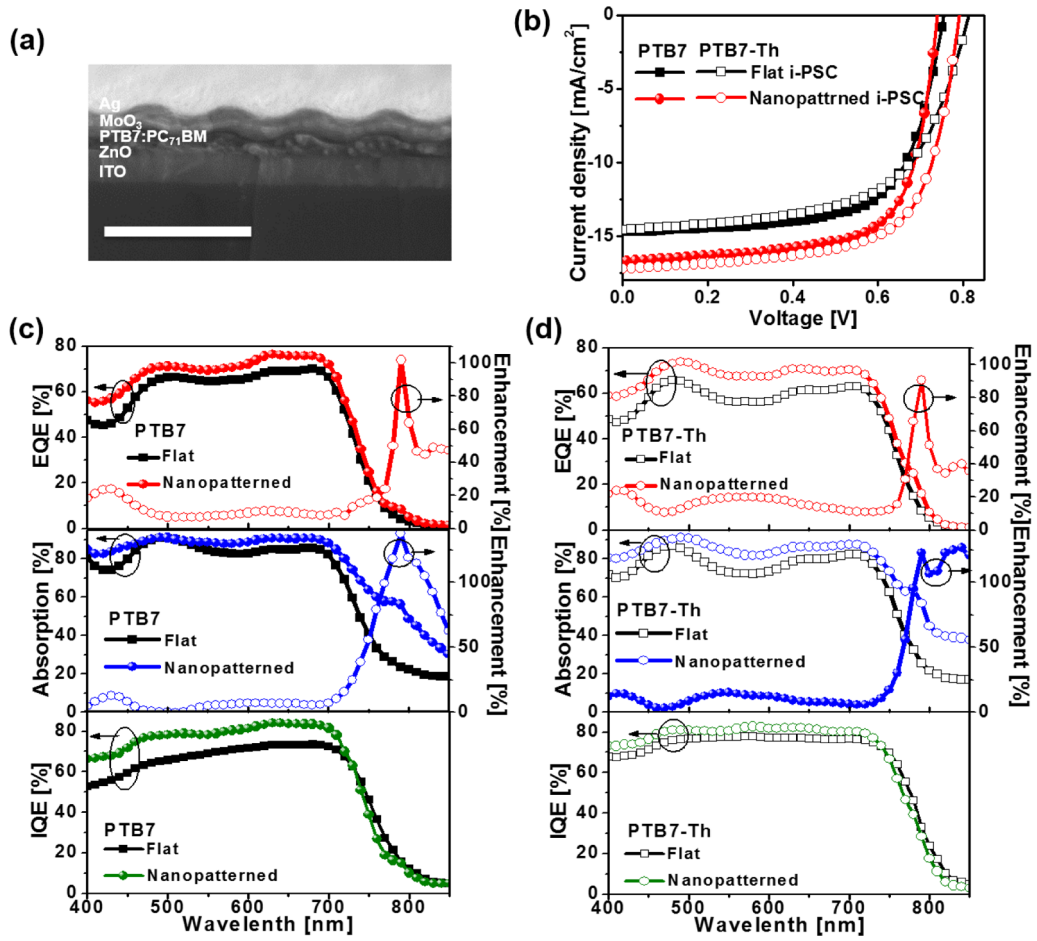

Figure 2. (a) The cross-sectional SEM image of a patterned i-PSC device with PTB7:$PC_{71}BM$. White scale bar: 500 nm. (b) $J-V$ characteristics of flat i-PSCs (black rectangles) and nanopatterned i-PSCs (red circles) with PTB7:$PC_{71}BM$ (filled) or PTB7-Th:$PC_{71}BM$ (open) under AM 1.5G 100 mW/cm^2 illumination. EQE spectra and EQE enhancement (top), absorption spectra and absorption enhancement (middle), and IQE spectra and IQE enhancement (bottom) of flat i-PSCs (rectangles) and nanopatterned i-PSCs (circles) with (c) PTB7:$PC_{71}BM$ (filled) or (d) PTB7-Th:$PC_{71}BM$ (open).

TABLE 1. Average Photovoltaic Performance of i-PSCs without or with Periodic Nanostructure[a]

active materials	performance	flat i-PSCs	nanopatterned i-PSCs
PTB7:$PC_{71}BM$	PCE [%]	7.33 ± 0.06 (7.40)	8.45 ± 0.05 (8.50)
	J_{sc} [mA/cm^2]	14.67 ± 0.15 (14.72)	16.37 ± 0.22 (16.30)
	V_{oc} [V]	0.75 ± 0.00 (0.75)	0.73 ± 0.01 (0.74)
	FF	0.68 ± 0.01 (0.67)	0.70 ± 0.01 (0.71)
PTB7-Th:$PC_{71}BM$	PCE [%]	7.15 ± 0.14 (7.17)	9.03 ± 0.12 (9.15)
	J_{sc} [mA/cm^2]	14.50 ± 0.23 (14.54)	17.22 ± 0.15 (17.21)
	V_{oc} [V]	0.81 ± 0.00 (0.81)	0.79 ± 0.00 (0.79)
	FF	0.61 ± 0.01 (0.61)	0.66 ± 0.01 (0.67)

[a] The ( ) illustrate the performance of devices having the highest PCEs. The average PCE values were obtained from 15 PTB7 based devices and 5 PTB7-Th based devices.

in Table 1. Current density vs voltage ($J-V$) characteristics of representative devices under AM 1.5G 100 mW/cm^2 are shown in Figure 2b. For all devices with a nanopatterned active layer composed of PTB7 and $PC_{71}BM$, the PCE was increased by approximately 15% with enhancement of both the short-circuit current density (J_{sc}) and fill factor (FF) of approximately 11% and 6%, respectively. The best PCE of flat control devices was 7.40% with a J_{sc} of 14.72 mA/cm^2, whereas the best PCE of devices with periodic nanostructures was 8.50%, mainly benefiting from the improved J_{sc} value of 16.30 mA/cm^2.

The proposed scheme is not limited to the PTB7:$PC_{71}BM$ system, but it can be applied to various BHJ systems consisting of polymer and fullerene derivative. For example, the introduction of periodic nanostructure to i-PSC with the active layer comprising PTB7-Th and $PC_{71}BM$ (Figure 2b) also enhanced the PCE significantly from 7.17% to 9.15% with enhancement of both J_{sc} and FF of approximately 18% and 10%, respectively. Detailed photovoltaic performance is summarized in Table 1.

To investigate the origin of the enhanced J_{sc} of the devices with periodic nanostructures in greater detail, we characterized EQE and absorption spectra of devices with and without the periodic nanostructures and estimated the enhancement factor of the EQE of the devices. The J_{sc} values were well matched (within 2% error) with the integrated J_{sc} values obtained from the EQE spectra. Compared with the flat device, EQE values for all nanopatterned devices were improved in an overall range from 350 to 900 nm with prominent enhancement at around 425 and 625 nm and a distinct peak in the NIR region, as shown in Figure 2c,d (top).

Absorption spectra were extracted from the measured reflectance spectra in the same setup as used for the EQE study, as shown in Figure 2c,d (middle). In the wide range of 400−850 nm, enhanced absorption is observed with distinct peaks at 400 and 550 nm, which can be ascribed to Wood's anomaly and localized surface plasmon modes near a grating.[31−34] In fact, the SPR peaks of films having a grating period of 556 nm appears experimentally at 935 nm (not shown), which is located outside the effective absorption range of PTB7:$PC_{71}BM$ from 300 to 850 nm, as shown in Figure 3c. In addition, absorption beyond the absorption edge of 750 nm is dramatically increased in the i-PSC with periodic nanostructures, compared to the flat i-PSC device. This could be related with increased charge transfer exciton (CTX) states as it is known that photocurrent near the absorption edge of the active layer in i-PSCs results from directly generated CTXs, although absorption in the range of the flat film is very weak.[24] The generation of CTXs can be influenced by the nanoscale morphology, as they are bound to the interfacial area of the BHJ system. We measured EQE under applied bias (4 V), which can collect the dissociated free charges that would otherwise recombine. Figure S1 in the Supporting Information demonstrates the enhanced EQE under bias in the nanopatterned i-PSC at the CT state energy region. The relatively low photocurrent was obtained despite the dramatically increased absorption beyond the absorption edge (~750 nm) due to inefficient dissociation of excitons by *direct* absorption of the CT state.[35,36]

To clarify the aforementioned effect on the electrical properties in the i-PSC with a periodic nanostructure in more detail, IQE was calculated from the relation EQE = absorption × IQE. As shown in Figure 2c,d (bottom), the device with the periodic nanostructure shows an enhanced IQE in the overall range except at around 800 nm of the band edge of PTB7 (and PTB7-Th), indicating an enhanced EQE in the i-PSC with nanostructures originated from dual improvement of absorption and IQE. The IQE value approaches approximately 85% in the visible range, suggesting that excitons are more effectively dissociated and relevant electrodes collect charge carriers efficiently with less recombination loss in the i-PSC with periodic nanostructures.

Along with the enhanced J_{sc} in i-PSCs with periodic nanostructures, the FF was also improved compared with that of the flat devices. The enhanced FF indicates improvement of electrical properties by the incorporation of periodic nanostructures in i-PSCs.[37] In particular, control of the nanomorphology can have a significant effect on the FF, because ordered and crystallized polymer chains increase charge carrier mobility and more finely intermixed donor and acceptor domains decrease exciton recombination and charge trapping. More detailed evidence of the optimized nanoscale morphology in the blend film by the incorporation of periodic nanostructures is discussed below.

In addition to the morphological change between electron donor and acceptor materials in the BHJ active layer, we also note that PDMS stamping can increase the interfacial area between the active layer and the contacted metal electrode slightly. With a depth of 40 nm and period of 556 nm, the interfacial area was increased by 12.2% for the nanostructured device. An extended interface between the active layer and the metal electrode can foster carrier extraction and decrease the series resistance of devices, leading to an improved FF.[6]

It has been widely recognized that the nanomorphology of a BHJ system largely influences separation of bound polaron pairs, CTXs into free charges at the junction between the PTB7 and $PC_{71}BM$ domains.[38,39] More finely intermixed PTB7 and $PC_{71}BM$ domains can result in an increased amount of CTXs, indicating elevated interaction between PTB7 and $PC_{71}BM$.[40] A nanoimprinting process can provide the driving force for finely intermixed PTB7 and $PC_{71}BM$ domains due to the surface confining effect by the mold, resulting in increased generation rate of CTXs at the donor/acceptor interface.[38,39]

To further verify the more finely intermixed PTB7 and $PC_{71}BM$ domains, the surface morphology of the active layer was investigated using a transmission electron microscope (TEM). Top-down TEM samples were prepared by floating the PTB7:$PC_{71}BM$ layers on deionized water and transferring the films to 300 mesh copper TEM grids. Figure 3a,b shows TEM images of a BHJ system composed of PTB7 and $PC_{71}BM$ without and with periodic nanostructures, respectively, measured at the same defocused imaging conditions of 25 μm.[21,41] The bright and dark regions result from the domain/network of polymer crystals and $PC_{71}BM$ domains, respectively. The TEM image of the PTB7:$PC_{71}BM$ layer with periodic nanostructures (Figure 3b) shows very fine and smaller PTB7 domains, suggesting increased interfacial area between PTB7 and $PC_{71}BM$, which favors the formation of CTXs.[42,43] The flat PTB7:$PC_{71}BM$ layer (Figure 3a), however, shows relatively larger phase-separated PTB7 and $PC_{71}BM$ domains.

Figure 3c shows the UV−vis absorption spectra of PTB7:$PC_{71}BM$ blend films both with and without

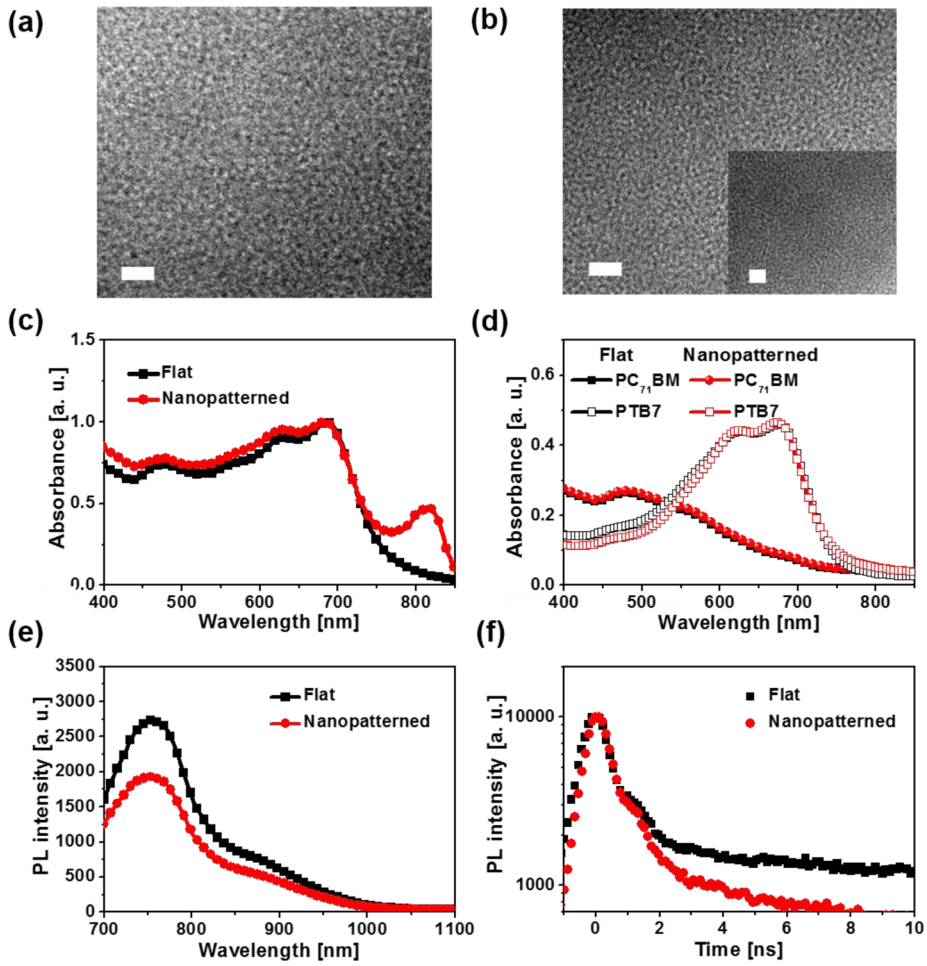

Figure 3. TEM images measured at the same defocusing distance of (a) flat PTB7:$PC_{71}BM$ surface and (b) ridge area of nanopatterned PTB7:$PC_{71}BM$ surface. (Inset, valley area of nanopatterned PTB7:$PC_{71}BM$ surface) White scale bar, 20 nm. UV−vis absorption spectra of (c) flat PTB7:$PC_{71}BM$ film (black rectangles) and nanopatterned PTB7:$PC_{71}BM$ film (red circles) and (d) pure PTB7 and $PC_{71}BM$ films with (open red circles) and without (filled black circles) periodic nanostructure. (e) Photoluminescence spectra excited at 533 nm for flat PTB7:$PC_{71}BM$ film (black rectangles) and nanopatterned PTB7:$PC_{71}BM$ film (red circles). (f) Time-resolved photoluminescence spectra; the emission at 750 nm was recorded after excitation at 633 nm. The time traces have been normalized to 10 000 counts.

periodic nanostructures. The absorption spectrum of the nanopatterned film exhibits a distinguishable absorption peak near 800 nm compared to the flat film, showing increased ordering of PTB7 chains and improved probability of CTX distribution across the PTB7 and $PC_{71}BM$ interfaces in the optimized morphology by the nanoimprinting process.[43,44] Interestingly, the prominent peak near 800 nm in the nanopatterned PTB7:$PC_{71}BM$ blend film was not observed in the PTB7 and $PC_{71}BM$ only films even with inclusion of the periodic nanopattern, suggesting that the additional peak resulted from interaction between PTB7 and $PC_{71}BM$ (Figure 3d).

Figure 3e shows that photoluminescence (PL) quenching, which supports exciton dissociation, is facilitated by more finely intermixed PTB7 and $PC_{71}BM$ domains in the active layer with the periodic nanostructure, as determined from the TEM characterization. In the nanopatterned PTB7:$PC_{71}BM$ film, the PL intensity at 750 nm corresponding to radiative decay of PTB7 when excited with a 633 nm laser source dramatically decreased, compared to the flat PTB7:$PC_{71}BM$ film, due to promoted exciton dissociation between PTB7 and $PC_{71}BM$.

In addition, the decay of emission at 750 nm is much faster in the nanopatterned PTB7:$PC_{71}BM$ film than in the flat PTB7:$PC_{71}BM$ film, as shown in Figure 3f and summarized in Table S1 in the Supporting Information. The PL decay curves were fitted using the multiexponential function: $\mathrm{IPL}(t) = A_1 \exp(-t/\tau_1) + A_2 \exp(-t/\tau_2)$, where A_i and τ_i are the amplitude and the exponential time constant, respectively.[45] For the flat PTB7:$PC_{71}BM$ film, two exponential time constants, τ_1 and τ_2, are obtained as 15.00 and 38.57 ps, respectively, providing intensity weighted average lifetime $\tau_{int} = 16.12$ ps. The nanopatterned PTB7:$PC_{71}BM$ film has faster constants of $\tau_1 = 9.70$ ps and $\tau_2 = 38.33$ ps from the remaining tail, resulting in a lower value of $\tau_{int} = 9.72$ ps. The reduced PL decay time is a result of more effective exciton dissociation in the nanopatterned PTB7:$PC_{71}BM$ film, indicative of better-intermixed morphology between

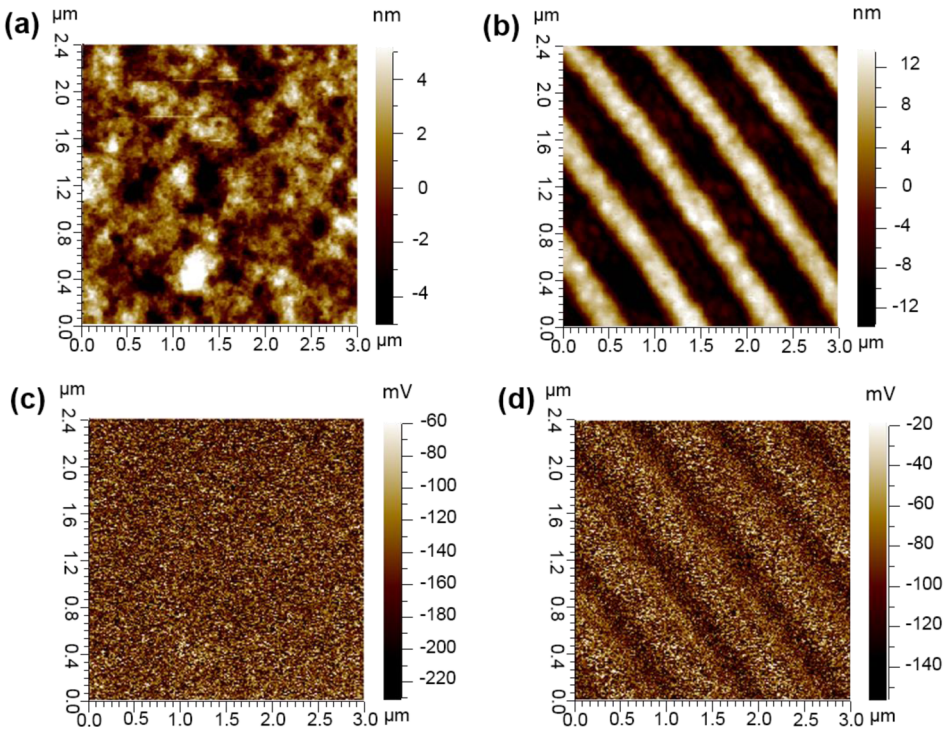

Figure 4. Surface topographic AFM images of (a) flat PTB7:$PC_{71}BM$ surface and (b) nanopatterned PTB7:$PC_{71}BM$ surface. KPFM-surface potential images of (c) flat PTB7:$PC_{71}BM$ surface and (d) nanopatterned PTB7:$PC_{71}BM$ surface.

PTB7 and $PC_{71}BM$ domains.[46] This is consistent with the TEM measurement, as shown in Figure 3a,b. The enhanced exciton dissociation led to a reduction of geminate recombination of photogenerated excitons and thereby enhanced the FF of the patterned device.[47]

To further examine the effect of the periodic nanostructure on the blend morphology, we measured the surface potential by Kelvin probe atomic force microscopy (KPFM), measuring the potential distribution of the flat and nanopatterned films, as shown in Figure 4. The average surface potential of the PTB7:$PC_{71}BM$ layer with periodic nanostructures (470 mV) was approximately 140 mV higher than that of the flat PTB7:$PC_{71}BM$ layer (330 mV). The surface potential is considerably influenced by surface conditions such as the surface charge density and chemical composition.[48,49] As shown in Figure 4d, a higher surface potential is associated with the relative position of the PTB7 crystallite structure aligned toward the surface by capillary force in the nanoimprinting, yielding effective charge extraction.[50] Under a confined cavity after a spin-coating process, fluidic PTB7 molecules with lower surface energy can flow and align toward the hydrophobic PDMS mold, causing a gradient of PTB7 in the vertical direction of the active layer region.[51] The surface tension for PTB7 (22.7 mN/m) is much smaller than that of $PC_{71}BM$ (31.1 mN/m), suggesting that PTB7 molecules would be preferentially positioned toward the top surface contacting with the PDMS mold with a surface tension of 24 mN/m. The contact angle and surface tension for the PTB7 and $PC_{71}BM$ were measured and are summarized in Table S2 in the Supporting Information. Interestingly, on the grooved films, a remarkable difference in the surface potential was observed between the ridge (520 mV) and valley (450 mV), resulting from ordered packing of PTB7 chains upward dominantly by the capillary force in the nanoimprinting process.[52] A dynamics secondary-ion mass spectroscopy (DSIMS) analysis was performed to determine the relative distribution of PTB7 and $PC_{71}BM$ across the vertical direction of the active layer (Figure S2 in the Supporting Information). The ^{32}S signal was monitored to observe the relative amount of PTB7 within the active layer. A vertical gradient of PTB7 was observed, providing preferential carriers paths to the electrodes.

To verify vertical phase segregation induced by the interaction between PTB7 molecules and the PDMS mold, a flat device pressured under a flat PDMS mold during a drying process was also fabricated. As shown in the DSIMS depth profile of Figure S2c in the Supporting Information, the ^{32}S signal of the pressured flat PTB7:$PC_{71}BM$ film increased gradually toward the top surface, additionally signifying PTB7 molecules were positioned near the top surface due to the attractive interaction between the hydrophobic PTB7 and the PDMS mold. Consequently, the EQE value increased in a broad band, mainly due to improved IQE compared to the flat device, while absorption showed little change, as presented in Figure S4 in the Supporting Information. As a result, enhanced performance was

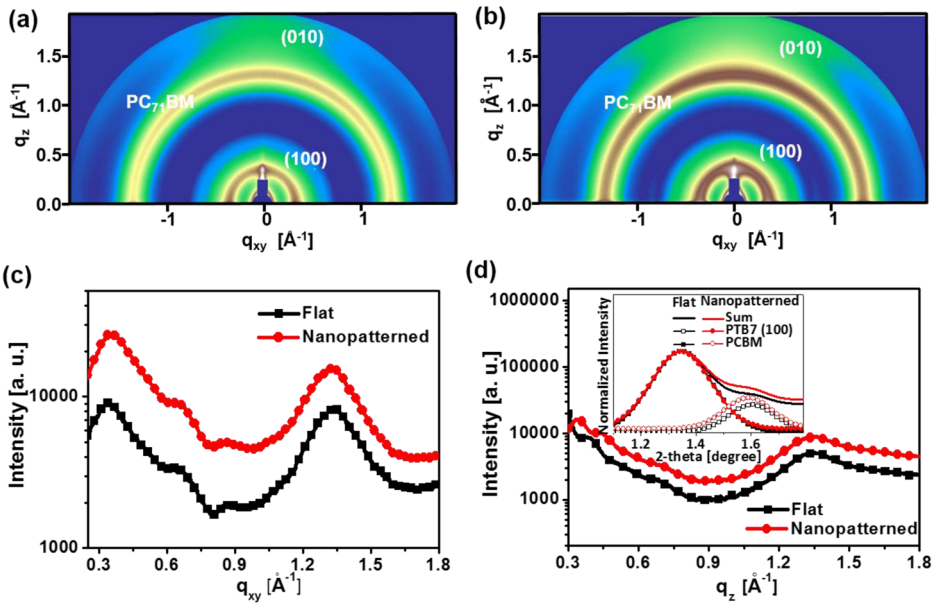

Figure 5. 2D GIWAXS profiles of PTB7:$PC_{71}BM$ film (a) without and (b) with periodic nanostructure. (c) In-plane GIWAXS profiles of flat PTB7:$PC_{71}BM$ film (black rectangles) and nanopatterned PTB7:$PC_{71}BM$ film (red circles). (d) Out-of-plane GIWAXS profiles of flat PTB7:$PC_{71}BM$ film (black rectangles) and nanopatterned PTB7:$PC_{71}BM$ film (red circles). (Inset, enlarged out-of-plane profiles in a range from 0.9 to 1.9 $Å^{-1}$ for PTB7:$PC_{71}BM$ film without (black rectangles) and with (red circles) a periodic nanostructure).

observed in the pressed device, with enhanced J_{sc}, as shown in Figure S3 in the Supporting Information. The enhancement (6.1%) was smaller than that of the nanopatterned device (10.7%). This result verifies that vertical phase segregation induced by the nanoimprinting process improved the IQE of the devices.

We performed grazing incidence wide angle X-ray scattering (GIWAXS) to clarify the effect of the nanoimprinting process on crystallization and chain alignment of the PTB7 polymer. Figure 5 compares 2D GIWAXS results of a nanopatterned PTB7:$PC_{71}BM$ layer with a flat layer. According to the 2D GIWAXS patterns in Figure 5a,b, the (100) scattering peak corresponding to periodic edge-on PTB7 lamellar shows ring-like patterns at around 0.35 $Å^{-1}$. In-plane scans in Figure 5c reveal that the peak intensity at around 0.35 $Å^{-1}$ of the nanopatterned PTB7:$PC_{71}BM$ layer dramatically increased, compared to that of the flat PTB7:$PC_{71}BM$ layer. Interestingly, the peak shifted from q_z = 0.34−0.36 $Å^{-1}$ upon the nanopatterned PTB7:$PC_{71}BM$ layer, indicating that the interstack spacing of PTB7 lamellar was reduced from 18.6 to 17.5 Å, indicative of more compact interdigitation of alkyl side chains in the confined mold cavity.[53]

In addition, (010) scattering peaks at 1.6 $Å^{-1}$ associated with $\pi-\pi$ stacking of PTB7 molecules also reveal enlarged crystalline domains of the nanopatterned PTB7:$PC_{71}BM$ layer. As shown in the inset of Figure 5d, (010) scattering peaks were extracted from the peaks that partially overlapped with the (311) Bragg diffraction peak of $PC_{71}BM$ at 1.35 $Å^{-1}$; the peaks were separated by fitting the experimental data to a multipeak Gaussian function in the region of q_z = 1.1−1.8 $Å^{-1}$ to determine the $\pi-\pi$ stacked crystalline size and domain spacing.[51,54] The $\pi-\pi$ stacked crystalline size was estimated and compared by calculations of the crystalline correlation length (D_{001}) of the polymers using the Scherrer equation.[54] The D_{001} value of the patterned PTB7:$PC_{71}BM$ layer (2.97 nm) is much larger than that of the flat PTB7:$PC_{71}BM$ layer (2.21 nm), indicating that the polymers in the patterned PTB7:$PC_{71}BM$ layer had stronger crystalline order. Interestingly, both the (100) and (010) peaks of PTB7 in the patterned PTB7:$PC_{71}BM$ layer had stronger angular distributions. For quantitative analysis, we calculated the intensity ratio (I_{out}/I_{in}) of the out-of-plane to in-plane PTB7 lamellar peaks (100), which can be considered as the edge-on PTB7 lamellar to face-on crystallite ratio.[55] For the nanopatterned PTB7:$PC_{71}BM$ layer, I_{out}/I_{in} was calculated to be 2.47, whereas the ratio of the flat PTB7:$PC_{71}BM$ layer was 1.05, indicating a higher degree of edge-on orientation. This result suggests that *multi*-directional chain alignment with respect to the substrate was induced by the capillary forces in the nanoimprinting process, which allows PTB7 to flow vertically and form lamellar along the surface of the mold.[30,53,56] Thus, the holes can be effectively collected through the patterned metal electrode. Furthermore, the increased interfacial area between the active layer and the metal electrode and enlarged size of crystalline domains can result in enhanced charge carrier mobility of the nanopatterned PTB7:$PC_{71}BM$ layer.[53] We also obtained GIWAXS patterns of flat PTB7:$PC_{71}BM$ layers pressured and dried under a flat PDMS mold as another control device. As shown in Figure S5c,d in the Supporting Information, the (100) scattering peak of the pressured PTB7:$PC_{71}BM$

layer did not increase as much as that of the nanopatterned films. This comparative study implies that the nanoimprinting process to form periodic nanostructures effectively induced vertical chain alignment of PTB7 molecules in addition to intrinsic face-on alignments. Figure 1a schematically summarizes the experimental results.

Indeed, hole mobility was dramatically improved, as shown in Figures S6 and S7 in the Supporting Information. Space charge limited current (SCLC) measurements have been used to determine hole mobility under steady state current in organic layers.[57] The hole-only devices were fabricated with a structure of an ITO/PEDOT:PSS (40 nm)/active layer with and without a periodic structure (100 nm)/MoO_3 (20 nm)/Ag (150 nm). The hole mobilities for the devices with and without periodic nanostructures were calculated to be 4.8×10^{-4} cm^2 V^{-1} s^{-1} and 1.7×10^{-3} cm^2 V^{-1} s^{-1}, respectively. These results demonstrate that the incorporation of periodic nanostructures in PSCs considerably increases the hole mobility, partly due to the enhanced degree of PTB7 molecular packing and an increase of the interfacial area between the active layer and the metal electrode and the shortened distance between PTB7 rich-domains and the metal electrode as a result of the vertical gradient of PTB7 induced by the nanoimprinting process, providing preferential carrier paths to the electrodes.

As the GIWAXS results suggested, the nanoimprinting process allows PTB7 chains to partially realign to be vertical to the substrate due to vertical flow of the chains into nanocavities, originating from the interaction between the hydrophobic fluorine-substituted side-chain of PTB7 and the hydrophobic PDMS mold, in contrast to the predominantly parallel chain alignment to the substrate in the control device.[53,54] This implies that the introduction of the periodic nanostructure into PSCs can produce enhanced conductivity in both the lateral and vertical directions, which induces more effective charge transport compared with that of the control device.

CONCLUSIONS

In summary, we characterized the nanomorphological changes of a PTB7:$PC_{71}BM$ BHJ film induced by the introduction of a periodic nanostructure on the film and obtained an efficient i-PSC with considerably improved electrical properties. The nanoimprinting process using a PDMS mold effectively optimized the nanomorphology including the crystallization, chain alignment, and phase separation in the BHJ film. These results suggest that capillary force applied in the nanoimprinting process can induce the formation of an effective interpenetrating network between the improved PTB7 crystalline structure and $PC_{71}BM$, and a vertical phase segregated nanomorphology that can be attributed to the effectively arranged PTB7-rich domains and $PC_{71}BM$-rich domains. These morphological changes by the nanoimprinting contribute to improvement of both J_{sc} and FF in i-PSCs.

METHODS

Mold Fabrication. A two-component elastomeric kit (Sylgard 184, Dow Corning) was used to prepare the PDMS mold with the standard mixing ratio of base and hardener, 10:1 by weight. The mixture was poured and spread onto the master mold with periodic, 556 nm line patterns (1800 Grooves/mm, Edmund optics) and cured at 80 °C for 1 h. The solidified PDMS mold was later peeled from the master mold.

Device Fabrication. The photovoltaic devices were fabricated on indium tin oxide (ITO) glass (10 Ω/sq) as follows. ITO glass was sequentially cleaned by ultrasonic treatment in a detergent, deionized water, isopropyl alcohol, and acetone and then dried in an oven for 30 min. The ITO glass was treated with O_2 plasma for 10 min, and a 40 nm-thick ZnO layer was spin-coated onto the ITO glass and annealed at 200 °C for 60 min in air. After the substrate was transferred into a nitrogen-filled glovebox, a 100 nm-thick BHJ layer was spin-coated from a solution of PTB7 (or PTB7-Th):$PC_{71}BM$ (25 mg/mL, 1:1.5 w/w) in chlorobenzene:1,8-diidoctane (DIO) (97:3 v/v). Simultaneously, the PDMS mold was placed on the slide glass with the patterned surface facing upward. The formed PTB7:$PC_{71}BM$ layer on the ZnO/ITO glass was turned over immediately, put in conformal contact with the PDMS mold, and dried at 70 °C for 20 min in the glovebox. The applied pressure on the PTB7:PC71BM film by the PDMS mold in the nanoimprinting process was calculated to 52.59 Pa. A MoO_3 layer (10 nm) and an Ag layer (100 nm) were sequentially deposited on top of the patterned PTB7:$PC_{71}BM$ layer through a shadow mask by thermal evaporation at 10^{-7} Torr. The active area for all the devices was defined as 15 mm^2 by a shadow mask.

Characterizations. Current density−voltage (J−V) characteristics were measured under irradiance of 100 mW/cm^2 from a 150 W Xe short arc lamp filtered by an air mass 1.5G filter with a solar simulator (PEC-L12, Peccell Technologies). The external quantum efficiency (EQE) results were acquired using a spectral measurement system (K3100 IQX, McScience Inc.). This system applied monochromatic light from a xenon arc lamp at 300 W filtered by a monochromator (Newport) and an optical chopper (MC 2000 Thorlabs). Device reflectance ($R_{cell}(\lambda)$) as a function of wavelength λ was measured as follows: the incident monochromic light is reflected in the device tilted at approximately 8° through an integration sphere. The reflected light is scattered in the integration sphere and collected by a photodetector located in the integration sphere. The absorption was extracted from the measured wavelength-dependent reflectance data. The internal quantum efficiency (IQE) as a function of wavelength λ was determined as follows: IQE (λ) = EQE (λ)/[1 − $R_{device}(\lambda)$]

To determine the surface potential of the patterned active layer, Kelvin probe force microscopy (KPFM, Agilent 5500, Agilent Technologies.) measurement was performed in standard KPFM mode, using a single platinum-coated tip in a N_2 atmosphere. Surface morphology of the patterned active layer was observed with a field emission scanning electron microscope (FE-SEM, FEI Sirion) and a field emission transmission electron microscope (FE-TEM, FEI Tecnai G2 f30 S-Twin, 300 keV). Optical absorption measurement of the flat and nanopatterned PTB7:PC71BM films on glass was performed using a UV−visible spectrophotometer (UV-3600, Shimadzu) equipped with a 60 mm diameter integrating sphere. Grazing incidence wide-angle X-ray scattering (GIWAXS) measurement was performed using X-rays with a wavelength of λ = 1.54 Å at the 8C1 beamline of the Pohang Accelerator Laboratory (PAL). Secondary ion mass spectrometry (SIMS, CAMECA IMS 7f magnetic sector

SIMS) signals were measured using 10 kV Cs^+ primary ions, detecting negative secondary ions from the center area, which was 175 μm × 175 μm in size. Photoluminescence (PL) quenching was observed for both flat and the nanopatterned PTB7:$PC_{71}BM$ films without a metal electrode using a Horiba Jobin Yvon NanoLog spectrophotometer. The PL lifetime was calculated according to nonlinear, least-squares and iterative fitting using SynPhoTimes software (version 5.1.3).

Conflict of Interest: The authors declare no competing financial interest.

Supporting Information Available: Description of experimental procedures and calculations and additional experimental and calculation results. This material is available free of charge via the Internet at http://pubs.acs.org.

Acknowledgment. We gratefully acknowledge the support from the New & Renewable Energy Core Technology Program of the Korea Institute of Energy Technology Evaluation and Planning (KETEP), granted financial resource from the Ministry of Trade, Industry & Energy (Grant No. 20133030000130), Graphene Materials and Components Development Program of MOTIE/KEIT (Grant 10044412), EEWS Research Project of the Office of the KAIST EEWS Initiative (Grant EEWS-2014-N01140052), and KAIST Institute for the NanoCentury. This research was also supported by the Global Frontier R&D Program on Center for Multiscale Energy System (Grant 2012M3A6A7055540), funded by the Korean Government.

REFERENCES AND NOTES

1. You, J.; Dou, L.; Yoshimura, K.; Kato, T.; Ohya, K.; Moriarty, T.; Emery, K.; Chen, C. C.; Gao, J.; Li, G.; Yang, Y. A Polymer Tandem Solar Cell with 10.6% Power Conversion Efficiency. *Nat. Commun.* **2013**, *4*, 1446.
2. Chen, H. Y.; Hou, J. H.; Zhang, S. Q.; Liang, Y. Y.; Yang, G. W.; Yang, Y.; Yu, L. P.; Wu, Y.; Li, G. Polymer Solar Cells with Enhanced Open-Circuit Voltage and Efficiency. *Nat. Photon.* **2009**, *3*, 649–653.
3. Li, Y. F. Molecular Design of Photovoltaic Materials for Polymer Solar Cells: Toward Suitable Electronic Energy Levels and Broad Absorption. *Acc. Chem. Res.* **2012**, *45*, 723–733.
4. Yang, X. N.; Loos, J.; Veenstra, S. C.; Verhees, W. J. H.; Wienk, M. M.; Kroon, J. M.; Michels, M. A. J.; Janssen, R. A. J. Nanoscale Morphology of High-Performance Polymer Solar Cells. *Nano Lett.* **2005**, *5*, 579–583.
5. Kim, Y.; Cook, S.; Tuladhar, S. M.; Choulis, S. A.; Nelson, J.; Durrant, J. R.; Bradley, D. D. C.; Giles, M.; McCulloch, I.; Ha, C. S.; et al. A Strong Regioregularity Effect in Self-Organizing Conjugated Polymer Films and High-Efficiency Polythiophene:Fullerene Solar Cells. *Nat. Mater.* **2006**, *5*, 197–203.
6. Guo, X. G.; Zhou, N. J.; Lou, S. J.; Smith, J.; Tice, D. B.; Hennek, J. W.; Ortiz, R. P.; Navarrete, J. T. L.; Li, S. Y.; Strzalka, J.; et al. Polymer Solar Cells with Enhanced Fill Factors. *Nat. Photon.* **2013**, *7*, 825–833.
7. Campoy-Quiles, M.; Ferenczi, T.; Agostinelli, T.; Etchegoin, P. G.; Kim, Y.; Anthopoulos, T. D.; Stavrinou, P. N.; Bradley, D. D. C.; Nelson, J. Morphology Evolution *via* Self-Organization and Lateral and Vertical Diffusion in Polymer:Fullerene Solar Cell Blends. *Nat. Mater.* **2008**, *7*, 158–164.
8. Peumans, P.; Uchida, S.; Forrest, S. R. Efficient Bulk Heterojunction Photovoltaic Cells using Small-Molecular-Weight Organic Thin Films. *Nature* **2003**, *425*, 158–162.
9. Vithanage, D. A.; Devizis, A.; Abramavicius, V.; Infahsaeng, Y.; Abramavicius, D.; MacKenzie, R. C. I.; Keivanidis, P. E.; Yartsev, A.; Hertel, D.; Nelson, J.; et al. Visualizing Charge Separation in Bulk Heterojunction Organic Solar Cells. *Nat. Commun.* **2013**, *4*, 2334.
10. He, Z.; Zhong, C.; Huang, X.; Wong, W.-Y.; Wu, H.; Chen, L.; Su, S.; Cao, Y. Simultaneous Enhancement of Open-Circuit Voltage, Short-Circuit Current Density, and Fill Factor in Polymer Solar Cells. *Adv. Mater.* **2011**, *23*, 4636–4643.
11. Weickert, J.; Dunbar, R. B.; Hesse, H. C.; Wiedemann, W.; Schmidt-Mende, L. Nanostructured Organic and Hybrid Solar Cells. *Adv. Mater.* **2011**, *23*, 1810–1828.
12. Kim, M.; Kim, J.-H.; Choi, H. H.; Park, J. H.; Jo, S. B.; Sim, M.; Kim, J. S.; Jinnai, H.; Park, Y. D.; Cho, K. Electrical Performance of Organic Solar Cells with Additive Assisted Vertical Phase Separation in the Photoactive Layer. *Adv. Energy Mater.* **2014**, *4*, 1300612.
13. Park, H. J.; Lee, J. Y.; Lee, T.; Guo, L. J. Advanced Heterojunction Structure of Polymer Photovoltaic Cell Generating High Photocurrent with Internal Quantum Efficiency Approaching 100%. *Adv. Energy Mater.* **2013**, *3*, 1135–1142.
14. Li, G.; Shrotriya, V.; Huang, J. S.; Yao, Y.; Moriarty, T.; Emery, K.; Yang, Y. High-Efficiency Solution Processable Polymer Photovoltaic Cells by Self-Organization of Polymer Blends. *Nat. Mater.* **2005**, *4*, 864–868.
15. Peet, J.; Cho, N. S.; Lee, S. K.; Bazan, G. C. Transition from Solution to the Solid State in Polymer Solar Cells Cast from Mixed Solvents. *Macromolecules* **2008**, *41*, 8655–8659.
16. Su, M. S.; Kuo, C. Y.; Yuan, M. C.; Jeng, U. S.; Su, C. J.; Wei, K. H. Improving Device Efficiency of Polymer/Fullerene Bulk Heterojunction Solar Cells through Enhanced Crystallinity and Reduced Grain Boundaries Induced by Solvent Additives. *Adv. Mater.* **2011**, *23*, 3315–3319.
17. Peet, J.; Kim, J. Y.; Coates, N. E.; Ma, W. L.; Moses, D.; Heeger, A. J.; Bazan, G. C. Efficiency Enhancement in Low-Bandgap Polymer Solar Cells by Processing with Alkane Dithiols. *Nat. Mater.* **2007**, *6*, 497–500.
18. Kim, K.-H.; Park, S.; Park, H. J.; Yu, H.; Kang, H.; Song, I.; Oh, J. H.; Kim, B. J. K. Determining Optimal Crystallinity of Diketopyrrolopyrrole-Based Terpolymers for Highly Efficient Polymer Solar Cells and Transistors. *Chem. Mater.* **2014**, *26*, 6963–6970.
19. Chu, C. W.; Yang, H. C.; Hou, W. J.; Huang, J. S.; Li, G.; Yang, Y. Control of the Nanoscale Crystallinity and Phase Separation in Polymer Solar Cells. *Appl. Phys. Lett.* **2008**, *92*, 103306.
20. Hammond, M. R.; Kline, R. J.; Herzing, A. A.; Richter, L. J.; Germack, D. S.; Ro, H. W.; Soles, C. L.; Fischer, D. A.; Xu, T.; Yu, L. P.; et al. Molecular Order in High-Efficiency Polymer/Fullerene Bulk Heterojunction Solar Cells. *ACS Nano* **2011**, *5*, 8248–8257.
21. Liang, Y. Y.; Xu, Z.; Xia, J. B.; Tsai, S. T.; Wu, Y.; Li, G.; Ray, C.; Yu, L. P. For the Bright Future-Bulk Heterojunction Polymer Solar Cells with Power Conversion Efficiency of 7.4%. *Adv. Mater.* **2010**, *22*, E135–E138.
22. Ferry, V. E.; Munday, J. N.; Atwater, H. A. Design Considerations for Plasmonic Photovoltaics. *Adv. Mater.* **2010**, *22*, 4794–4808.
23. Na, S. I.; Kim, S. S.; Jo, J.; Oh, S. H.; Kim, J.; Kim, D. Y. Efficient Polymer Solar Cells with Surface Relief Gratings Fabricated by Simple Softlithography. *Adv. Funct. Mater.* **2008**, *18*, 3956–3963.
24. Kim, J. B.; Kim, P.; Pegard, N. C.; Oh, S. J.; Kagan, C. R.; Fleischer, J. W.; Stone, H. A.; Loo, Y. L. Wrinkles and Deep Folds as Photonic Structures in Photovoltaics. *Nat. Photon.* **2012**, *6*, 327–332.
25. Haug, F. J.; Soderstrom, T.; Cubero, O.; Terrazzoni-Daudrix, V.; Ballif, C. Plasmonic Absorption in Textured Silver Back Reflectors of Thin Film Solar Cells. *J. Appl. Phys.* **2008**, *104*, 064509.
26. Abass, A.; Shen, H. H.; Bienstman, P.; Maes, B. Angle Insensitive Enhancement of Organic Solar Cells using Metallic Gratings. *J. Appl. Phys.* **2011**, *109*, 023111.
27. Aryal, M.; Trivedi, K.; Hu, W. C. Nano-Confinement Induced Chain Alignment in Ordered P3HT Nanostructures Defined by Nanoimprint Lithography. *ACS Nano* **2009**, *3*, 3085–3090.
28. Liang, X. G.; Chen, T.; Jung, Y. S.; Miyamoto, Y.; Han, G.; Cabrini, S.; Ma, B. W.; Olynick, D. L. Nanoimprint-Induced Molecular Stacking and Pattern Stabilization in a Solution-Processed Subphthalocyanine Film. *ACS Nano* **2010**, *4*, 2627–2634.
29. Steward, P. A.; Hearn, J.; Wilkinson, M. C. An Overview of Oolymer Latex Film Formation and Properties. *Adv. Colloid Interface Sci.* **2000**, *86*, 195–267.

30. Xie, F. X.; Choy, W. C. H.; Zhu, X. L.; Li, X. L.; Li, Z.; Liang, C. J. Improving Polymer Solar Cell Performances by Manipulating the Self-Organization of Polymer. *Appl. Phys. Lett.* **2011**, *98*, 023111.
31. Angelskar, H.; Johansen, I. R.; Lacolle, M.; Sagberg, H.; Sudbo, A. S. Spectral Uniformity of Two- and Four-Level Diffractive Optical Elements for Spectroscopy. *Opt. Express* **2009**, *17*, 10206–10222.
32. Sha, W. E. I.; Choy, W. C. H.; Chew, W. C. Angular Response of Thin-Film Organic Solar Cells with Periodic Metal Back Nanostrips. *Opt. Lett.* **2011**, *36*, 478–480.
33. Heine, C.; Morf, R. H. Submicrometer Gratings for Solar-Energy Applications. *Appl. Opt.* **1995**, *34*, 2476–2482.
34. Li, X. H.; Choy, W. C. H.; Huo, L. J.; Xie, F. X.; Sha, W. E. I.; Ding, B. F.; Guo, X.; Li, Y. F.; Hou, J. H.; You, J. B.; et al. Dual Plasmonic Nanostructures for High Performance Inverted Organic Solar Cells. *Adv. Mater.* **2012**, *24*, 3046–3052.
35. Vandewal, K.; Tvingstedt, K.; Gadisa, A.; Inganas, O.; Manca, J. V. On the Origin of the Open-Circuit Voltage of Polymer-Fullerene Solar Cells. *Nat. Mater.* **2009**, *8*, 904–909.
36. Bakulin, A. A.; Rao, A.; Pavelyev, V. G.; van Loosdrecht, P. H. M.; Pshenichnikov, M. S.; Niedzialek, D.; Cornil, J.; Beljonne, D.; Friend, R. H. The Role of Driving Energy and Delocalized States for Charge Separation in Organic Semiconductors. *Science* **2012**, *335*, 1340–1344.
37. Li, G.; Zhu, R.; Yang, Y. Polymer Solar Cells. *Nat. Photon.* **2012**, *6*, 153–161.
38. Albrecht, S.; Vandewal, K.; Tumbleston, J. R.; Fischer, F. S. U.; Douglas, J. D.; Frechet, J. M. J.; Ludwigs, S.; Ade, H.; Salleo, A.; Neher, D. On the Efficiency of Charge Transfer State Splitting in Polymer:Fullerene Solar Cells. *Adv. Mater.* **2014**, *26*, 2533–2539.
39. Vandewal, K.; Albrecht, S.; Hoke, E. T.; Graham, K. R.; Widmer, J.; Douglas, J. D.; Schubert, M.; Mateker, W. R.; Bloking, J. T.; Burkhard, G. F.; et al. Efficient Charge Generation by Relaxed Charge-Transfer States at Organic Interfaces. *Nat. Mater.* **2014**, *13*, 63–68.
40. Jailaubekov, A. E.; Willard, A. P.; Tritsch, J. R.; Chan, W.-L.; Sai, N.; Gearba, R.; Kaake, L. G.; Williams, K. J.; Leung, K.; Rossky, P. J.; et al. Hot Charge-Transfer Excitons set the Time Limit for Charge Separation at Donor/Acceptor Interfaces in Organic Photovoltaics. *Nat. Mater.* **2013**, *12*, 66–73.
41. Moon, J. S.; Lee, J. K.; Cho, S. N.; Byun, J. Y.; Heeger, A. J. "Columnlike" Structure of the Cross-Sectional Morphology of Bulk Heterojunction Materials. *Nano Lett.* **2009**, *9*, 230–234.
42. Osikowicz, W.; de Jong, M. P.; Salaneck, W. R. Formation of the Interfacial Dipole at Organic-Organic Interfaces: C60/Polymer Interfaces. *Adv. Mater.* **2007**, *19*, 4213–4217.
43. Vandewal, K.; Widmer, J.; Heumueller, T.; Brabec, C. J.; McGehee, M. D.; Leo, K.; Riede, M.; Salleo, A. Increased Open-Circuit Voltage of Organic Solar Cells by Reduced Donor-Acceptor Interface Area. *Adv. Mater.* **2014**, *26*, 3839–3843.
44. Vandewal, K.; Gadisa, A.; Oosterbaan, W. D.; Bertho, S.; Banishoeib, F.; Van Severen, I.; Lutsen, L.; Cleij, T. J.; Vanderzande, D.; Manca, J. V. The Relation between Open-Circuit Voltage and the Onset of Photocurrent Generation by Charge-Transfer Absorption in Polymer:Fullerene Bulk Heterojunction Solar Cells. *Adv. Funct. Mater.* **2008**, *18*, 2064–2070.
45. Jones, M.; Nedeljkovic, J.; Ellingson, R. J.; Nozik, A. J.; Rumbles, G. Photoenhancement of Luminescence in Colloidal CdSe Quantumdot Solutions. *J. Phys. Chem. B* **2003**, *107*, 11346–11352.
46. Hedley, G. J.; Ward, A. J.; Alekseev, A.; Howells, C. T.; Martins, E. R.; Serrano, L. A.; Cooke, G.; Ruseckas, A.; Samuel, I. D. W. Determining the Optimum Morphology in High-Performance Polymer-Fullerene Organic Photovoltaic Cells. *Nat. Commun.* **2013**, *4*, 2867.
47. Moet, D. J. D.; Lenes, M.; Morana, M.; Azimi, H.; Brabec, C. J.; Blom, P. W. M. Enhanced Dissociation of Charge-Transfer States in Narrow Band Gap Polymer:Fullerene Solar Cells Processed with 1,8-Octanedithiol. *Appl. Phys. Lett.* **2010**, *96*, 213506.
48. Zhou, H. Q.; Zhang, Y.; Seifter, J.; Collins, S. D.; Luo, C.; Bazan, G. C.; Nguyen, T. Q.; Heeger, A. J. High-Efficiency Polymer Solar Cells Enhanced by Solvent Treatment. *Adv. Mater.* **2013**, *25*, 1646–1652.
49. Pingree, L. S. C.; Reid, O. G.; Ginger, D. S. Electrical Scanning Probe Microscopy on Active Organic Electronic devices. *Adv. Mater.* **2009**, *21*, 19–28.
50. Spadafora, E. J.; Demadrille, R.; Ratier, B.; Grevin, B. Imaging the Carrier Photogeneration in Nanoscale Phase Segregated Organic Heterojunctions by Kelvin Probe Force Microscopy. *Nano Lett.* **2010**, *10*, 3337–3342.
51. Szarko, J. M.; Guo, J. C.; Liang, Y. Y.; Lee, B.; Rolczynski, B. S.; Strzalka, J.; Xu, T.; Loser, S.; Marks, T. J.; Yu, L. P.; et al. When Function Follows Form: Effects of Donor Copolymer Side Chains on Film Morphology and BHJ Solar Cell Performance. *Adv. Mater.* **2010**, *22*, 5468–5472.
52. Tsoi, W. C.; Spencer, S. J.; Yang, L.; Ballantyne, A. M.; Nicholson, P. G.; Turnbull, A.; Shard, A. G.; Murphy, C. E.; Bradley, D. D. C.; Nelson, J.; et al. Effect of Crystallization on the Electronic Energy Levels and Thin Film Morphology of P3HT:PCBM Blends. *Macromolecules* **2011**, *44*, 2944–2952.
53. Kline, R. J.; McGehee, M. D.; Toney, M. F. Highly Oriented Crystals at the Buried Interface in Polythiophene Thin-Film Transistors. *Nat. Mater.* **2006**, *5*, 222–228.
54. Guo, J. C.; Liang, Y. Y.; Szarko, J.; Lee, B.; Son, H. J.; Rolczynski, B. S.; Yu, L. P.; Chen, L. X. Structure, Dynamics, and Power Conversion Efficiency Correlations in a New Low Bandgap Polymer: PCBM Solar Cell. *J. Phys. Chem. B* **2010**, *114*, 742–748.
55. Osaka, I.; Saito, M.; Koganezawa, T.; Takimiya, K. Thiophene-Thiazolothiazole Copolymers: Significant Impact of Side Chain Composition on Backbone Orientation and Solar Cell Performances. *Adv. Mater.* **2014**, *26*, 331–338.
56. Chen, W.; Xu, T.; He, F.; Wang, W.; Wang, C.; Strzalka, J.; Liu, Y.; Wen, J. G.; Miller, D. J.; Chen, J. H.; et al. Hierarchical Nanomorphologies Promote Exciton Dissociation in Polymer/Fullerene Bulk Heterojunction Solar Cells. *Nano Lett.* **2011**, *11*, 3707–3713.
57. Chirvase, D.; Chiguvare, Z.; Knipper, M.; Parisi, J.; V, D.; Hummelen, J. C. Temperature Dependent Characteristics of Poly(3-hexylthiophene)-Fullerene Based Heterojunction Organic Solar Cells. *J. Appl. Phys.* **2003**, *93*, 3376–3383.